

MUJICA: Reforming SISR Models for PBR Material Super-Resolution via Cross-Map Attention

Xin Du¹, Maoyuan Xu^{1*}, Zhi Ying¹

¹Ubisoft La Forge

goldenbiglord@gmail.com, mao-yuan.xu@ubisoft.com, zhi.ying@ubisoft.com

Abstract

Physically Based Rendering (PBR) materials are typically characterized by multiple 2D texture maps such as basecolor, normal, metallic, and roughness which encode spatially-varying bi-directional reflectance distribution function (SVBRDF) parameters to model surface reflectance properties and microfacet interactions. Upscaling SVBRDF material is valuable for modern 3D graphics applications. However, existing Single Image Super-Resolution (SISR) methods struggle with cross-map inconsistency, inadequate modeling of modality-specific features, and limited generalization due to data distribution shifts. In this work, we propose **Multi-modal Upscaling Joint Inference via Cross-map Attention (MUJICA)**, a flexible adapter that reforms pre-trained Swin-transformer-based SISR models for PBR material super-resolution. MUJICA is seamlessly attached after the pre-trained and frozen SISR backbone. It leverages cross-map attention to fuse features while preserving remarkable reconstruction ability of the pre-trained SISR model. Applied to SISR models such as SwinIR, DRCT and HMANet, MUJICA improves PSNR, SSIM, and LPIPS scores while preserving cross-map consistency. Experiments demonstrate that MUJICA enables efficient training even with limited resources and delivers state-of-the-art performance on PBR material datasets.

Introduction

Physically Based Rendering (PBR) materials consist of different 2D texture maps such as basecolor, normal, roughness and metallic, that describe the appearance of virtual 3D shapes under arbitrary lighting in the form of spatially-varying bi-directional reflectance distribution function (SVBRDF). The industry continues to explore ways to integrate deep learning methods into modern PBR material production pipeline for various reasons. One major motivation is the requirement to upscale low-resolution legacy PBR materials to a higher resolution when developing remastered versions of games. Since legacy assets were created without using tools like Adobe Substance 3D Sampler, it is usually not possible to regenerate at arbitrary resolution. Another key factor is the growing adoption of diffusion models (Podell et al. 2023; Ho, Jain, and Abbeel 2020; Sohl-Dickstein et al. 2015; Song and Ermon 2019; Song et al.

2020) to generate high-quality PBR materials (Vecchio et al. 2024a; Ye et al. 2024; Saravanan et al. 2025; Vecchio et al. 2024b; Esser et al. 2024). However, the native output resolution of these models is typically limited to 512×512 or 1024×1024 in current industrial practice due to limited computation resources, failing to reach industrial requirements such as 4096×4096 . Therefore, reconstructing high-resolution PBR materials from low-resolution inputs has become an important component of modern industry pipelines.

In the task of Single Image Super-Resolution (SISR), methods based on Swin Transformer (Liu et al. 2021) have achieved remarkable success over CNN-based methods (Ledig et al. 2017b; Lim et al. 2017; Li et al. 2020; Wang et al. 2018; Zhang et al. 2018b), but their direct application to PBR materials faces three main limitations:

- **Cross-Map Inconsistency.** As shown in fig. 1 (a), SISR models process each PBR material map such as basecolor and normal separately, breaking consistency between maps. Such map inconsistency results in inconsistent renderings under varying lighting conditions.
- **Texture Distortion.** Figure 1 (b) demonstrates that directly applying pre-trained state-of-the-art (SOTA) SISR models to PBR materials produces incorrect results like texture distortion. This is mostly due to the different data distribution between the natural images that SISR models are trained on and the PBR materials.
- **Limited Datasets.** Available datasets for training PBR material super-resolution (SR) models are much more limited compared with those for SISR. To train our model, we employ MatSynth (Vecchio and Deschaintre 2024), the only publicly available SVBRDF dataset for our task, along with our in-house dataset. Remarkably, the textural and compositional complexity in single natural image often significantly surpasses single PBR material as shown in fig. 1 (c). Hence, training a PBR material SR model with limited data resources presents a significant challenge.

To address the challenges above, we propose **Multi-modal Upscaling Joint Inference via Cross-map Attention (MUJICA)** in this paper to adapt SOTA SISR models like SwinIR (Liang et al. 2021), DRCT (Hsu, Lee, and Chou 2024) and HMANet (Chu et al. 2024) to PBR material SR task by cross-map feature fusion. To better capture the intri-

*Corresponding author.

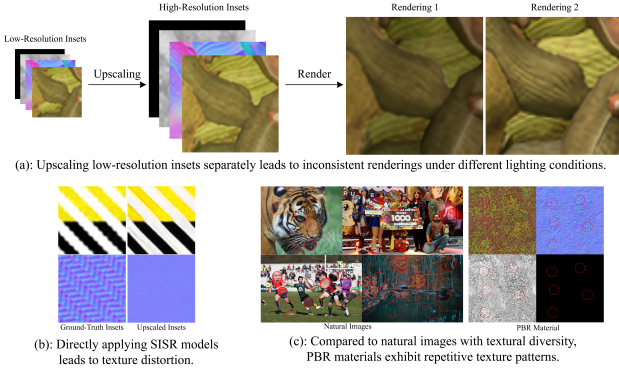


Figure 1: Limitations of directly applying SISR models on PBR materials.

cate interdependence among different PBR material maps, MUJICA adopts an attention-based fusion strategy. This design allows for both shared representation learning and flexible map specific refinement, facilitating robust multi-modal modeling under the complex structural priors inherent in PBR materials. Our contributions are summarized as below

- **Multi-modal Upscaling.** MUJICA reformulates PBR material SR as a multi-modal fusion problem, achieving SOTA performance on existing PBR material datasets.
- **Adapter for SISR models.** MUJICA as an adapter to reform existing Swin-transformer-based SISR models to multi-modal SR models. Equipped with MUJICA, existing SISR models have the ability to deal with PBR materials while keeping their remarkable performance.
- **Efficient Training.** By integrating MUJICA with any frozen, pre-trained Swin-transformer-based SISR model as the backbone, only a small number of parameters need to be trained. Therefore, our proposed method can keep training requirements and hardware demands at a relatively low level while achieving SOTA performance even with limited training data.

Experiments demonstrate that MUJICA achieves SOTA performance on existing PBR material datasets. For $\times 2$ SR task, MUJICA outperforms their SISR backbones with gains of up to **1.15dB** in PSNR, **0.0069** in SSIM, and a reduction of **0.036** in LPIPS on renderings across datasets. For $\times 4$ SR task, MUJICA improves metrics up to **0.76dB** in PSNR, **0.0070** in SSIM, and **0.0695** in LPIPS.

Related Work

Single Image Super-Resolution

In SISR task, transformer-based SISR methods (Zhou et al. 2023; Chen et al. 2023b; Liang et al. 2021; Hsu, Lee, and Chou 2024; Chu et al. 2024) achieve better performance than traditional CNN-based methods (Ledig et al. 2017b; Lim et al. 2017; Li et al. 2020; Wang et al. 2018; Zhang et al. 2018b).

Swin-transformer-based Method. SwinIR (Liang et al. 2021), a classic Swin-transformer-based (Vaswani et al.

2017; Liu et al. 2021) SISR model, performs self-attention within 8×8 local windows to extract deep features that significantly helps improve reconstructed high-resolution results. DRCT (Hsu, Lee, and Chou 2024) adds dense-connections (Huang et al. 2017) inside its residual blocks based on the architecture of SwinIR to mitigate the spatial information vanishing in deep feature extraction modules. HMANet (Chu et al. 2024) aims to extract self-similarity of images, including local similarity between nearby regions and global similarity across distant areas, by adding grid-attention to window-based self-attention mechanism.

GAN-based Method. Although GAN-based (Wang et al. 2018; Ledig et al. 2017a; Wu et al. 2017; Zhang et al. 2021) methods are able to generate visually richer textures, the adversarial loss tends to encourage the generator to produce plausible-looking details (Ledig et al. 2017a; Zhang et al. 2018a), even if those details contradict the ground-truth. To alleviate this problem, ESRGAN (Wang et al. 2018) introduces pixel-wise loss in its loss function, but structure distortions and hallucinated details still exist demonstrated by fig. 2.

Diffusion-based Method. Same situation happens to diffusion-based SISR models (Li et al. 2022; Saharia et al. 2022; Yue, Wang, and Loy 2023; Shang et al. 2024; Yue, Liao, and Loy 2025; Wang et al. 2024). Those models require iterative noise injection and denoising when predicting high-resolution images, which tends to alter images structure and details. The diffusion process mechanism could break the alignment across different material maps, making it less suitable for PBR material super-resolution task.

Considering the importance of both pixel-level accuracy and cross-map alignment in PBR material SR task, we adopt Swin-transformer-based architectures as our backbones.



Figure 2: Visual comparison on a natural image inset. ESRGAN and InvSR produce perceptually sharper textures but introduce structural distortions, while Swin-transformer-based method demonstrates superior capability in preserving accurate structural details.

PBR Material Super-Resolution

PBR material SR is a challenging problem due to the unique constraints of material maps, requiring strict cross-map consistency, and presenting structural patterns distinct from natural images. These factors have limited extensive research on this topic. Recently, MatUp (Gauthier et al. 2024) attempts to address PBR material SR by leveraging SOTA SISR models. It generates pseudo ground-truth through SOTA SISR models, which subsequently supervise a multilayer perceptron (MLP) via render loss. However, MatUp

suffers from two key limitations when applying to real-world PBR material SR task:

- MatUp trains a dedicated MLP model for each material at inference time. This process is time-consuming and limits generalization.
- The simple architecture of the MLP struggles to capture the complexity of PBR material SR task, making outputs quality significantly below the pseudo ground-truth generated by SISR models.

PBR-SR (Chen et al. 2025), another PBR material SR method, aims to utilize pre-trained SISR models in a similar way as MatUp to upscale mesh textures. However, it remains a mesh-specific model, making its practical application computationally expensive. Similarly to MatUp, PBR-SR suffers from the inherent limitation that the quality of its outputs cannot surpass that of the high-resolution pseudo ground-truth generated by the pre-trained SISR model.

As opposed to MatUp and PBR-SR, which require training a dedicated model or optimization process for each material, our MUJICA approach offers superior generalization with material-agnostic capabilities, enabling efficient and scalable applications across diverse PBR materials in industrial applications.

Multi-Modal Fusion

Traditionally, multi-modal fusion strategies are classified, based on the stage at which fusion occurs (Snoek, Worring, and Smeulders 2005; Gunes and Piccardi 2005; Li and Tang 2024; Baltrušaitis, Ahuja, and Morency 2018; Boulahia et al. 2021; Guarrasi et al. 2025), as early fusion, intermediate fusion, and late fusion.

Early fusion, also referred as data-level fusion, involves a simple concatenation of different modalities as input to form a shared feature subspace. Besides, early fusion prefers single-stream architecture (Gauthier et al. 2024; Zhang et al. 2023; Zhao et al. 2020; Zhang et al. 2020). For example, SuperYOLO (Zhang et al. 2023) employs pixel-wise concatenation between infrared images and RGB images to enhance super-resolution performance, improving object detection accuracy. MatUp (Gauthier et al. 2024) also adopts this data-level fusion, however, it does not perform optimally, because PBR materials are rendered according to complex rendering functions like SVBRDF and exhibit intricate interdependence that may not naturally align in the image space. For instance, a wrinkled white paper may have a highly detailed normal map while its basecolor map remains nearly uniform white. Such scenarios require more sophisticated modeling of modal interactions. Simply concatenating them at input level may ignore the difference between different modalities and fail to capture the comprehensive cross-map interaction.

Recent study (Guo et al. 2024; Tsai et al. 2019) demonstrates that feature-level attention-based fusion strategy with two-stream architecture often outperforms early fusion in tasks of loosely coupled or heterogeneous modalities.

In this work, we employ an intermediate fusion strategy by first performing cross-modal interactions, followed by modality-specific feature extraction to preserve and refine distinct characteristics.

Method

In this section, $m \in \mathcal{M}$ is defined as different PBR material map such as basecolor, normal, roughness and metallic, where \mathcal{M} denotes a collection of all maps of the PBR material. n is the PBR material map in set $\mathcal{M} \setminus \{m\}$ to provide complementary features. In this paper, each map is considered as an independent modality of the PBR material to better modeling the task.

As shown in fig. 3, our network consists of 5 modules. Among them, Shallow and Deep Feature Extraction, along with the HQ Image Reconstruction modules, are frozen during training. In contrast, Cross-Map Feature Fusion and Fused Feature Extraction modules, called MUJICA, are trainable adapter modules.

Overall Architecture

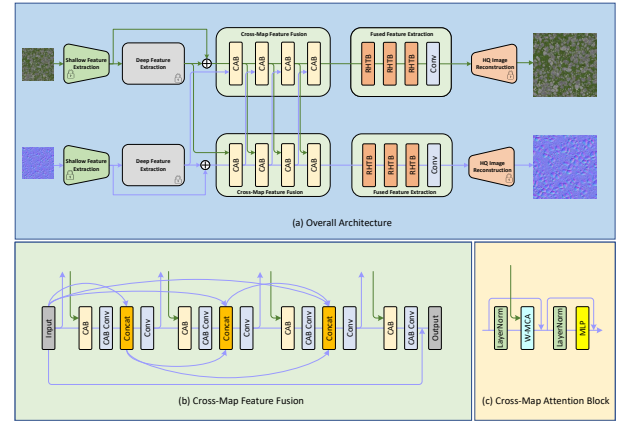


Figure 3: Architecture overview. (a) Illustration of the interaction between **basecolor** and **normal** modalities. The lock symbol indicates modules that are frozen during training. (b) and (c) only display of the **normal** modality.

Shallow and Deep Feature Extraction. Given a low-resolution (LR) input $\mathbf{I}_{LR}^m \in \mathbb{R}^{H \times W \times C_{in}}$ (H , W and C_{in} are the image height, width and input channel number, respectively) for $m \in \mathcal{M}$, the shallow feature $\mathbf{F}_0^m \in \mathbb{R}^{H \times W \times C}$ is extracted by a shared 3×3 convolutional layer (Xiao et al. 2021) $\text{Conv}(\cdot)$, where C is the feature channel number.

\mathbf{F}_0^m is then passed through a shared deep Swin-transformer-based backbone $H_{DF}(\cdot)$ to obtain modality-specific deep feature \mathbf{F}_{DF}^m . The resulting deep feature captures rich spatial information essential for texture and detail reconstruction.

Cross-Map Feature Fusion. To enhance the modality-specific feature \mathbf{F}_{Fused}^m with cross-modality context, we propose the Cross-Map Feature Fusion module, consisting of L stacked Cross-Map Attention Blocks (CABs), denoted as $\{B_i^m\}_{i=1}^L$. At each layer, features of modality m are refined using both self and other modality features. The fusion process is formulated as

$$\mathbf{F}_{Fused}^m = H_{FF}^m(\mathbf{F}_{DF}^m + \mathbf{F}_0^m, \mathbf{F}_{DF}^n),$$

where $H_{FF}(\cdot, \cdot)$ denotes the feature fusion module for modality m ; the external set $\{\mathbf{F}_{DF}^n\}$ provides complementary features from other modalities to enhance the representation of modality m .

Fused Feature Extraction. After Cross-Map Feature Fusion module, the modality-specific representation is further enhanced by applying a sequence of residual transformer blocks. These blocks are designed to extract features from \mathbf{F}_{Fused}^m . For a given modality m , the extracted fused feature \mathbf{F}_{FEE}^m is calculated by $H_{FEE}^m(\mathbf{F}_{Fused}^m)$, where $H_{FEE}^m(\cdot)$ denotes the modality-specific Fused Feature Extraction module.

HQ Image Reconstruction. The high-quality super-resolution (SR) image I_{SR}^m for modality m is reconstructed from \mathbf{F}_{FEE}^m using a shared reconstruction module $H_{rec}(\cdot)$, where $H_{rec}(\cdot)$ is implemented using pixel shuffle and convolutional layers.

Cross-Map Feature Fusion

The Cross-Map Feature Fusion module comprises L stacked Cross-Map Attention Blocks (CABs) B_l , with each performing layer-wise interaction between modality m and n . Inspired by DRCT (Hsu, Lee, and Chou 2024) which demonstrates that, compared to residual connections, dense connections better preserve high-frequency features during cross-map feature fusion. Hence, a dense connection strategy is adopted in this module to progressively concatenate intermediate features before passing them to next CAB.

Different from previous multi-modal fusion methods which typically perform cross-modal interaction only at selected stages, our proposed Cross-Map Feature Fusion module emphasizes progressive and layer-wise fusion. Within each CAB, modality features are iteratively refined using complementary context from other modalities, allowing proposed network to gradually align different PBR map features. Let $x_l^m \in \mathbb{R}^{H \times W \times C}$ denote the feature of the given modality m produced by l -th CAB, the whole cross-map feature fusion process is formulated as

$$\begin{aligned} x_1^m &= B_1^m([\mathbf{F}_{DF}^m + \mathbf{F}_0^m], \mathbf{F}_{DF}^n), \\ x_2^m &= B_2^m([\mathbf{F}_{DF}^m + \mathbf{F}_0^m, H_1^m(x_1^m)], x_1^n), \\ &\dots, \\ x_L^m &= B_L^m([\mathbf{F}_{DF}^m + \mathbf{F}_0^m, H_1^m(x_1^m), \dots, H_{L-1}^m(x_{L-1}^m)], \\ &\quad x_{L-1}^n), \end{aligned}$$

where $[\cdot, \dots, \cdot]$ denotes the concatenation of features; for $i \in \{1, 2, \dots, L-1\}$, $H_i^m(\cdot)$, a transition function to reduce the dimensionality of the previous layers' outputs and prevent feature explosion, is implemented as a 1×1 convolutional layer along with a LeakyReLU (Xu et al. 2015) with negative slope of 0.2. Despite the progressive dense fusion and repeated cross-map attention, our proposed CAB maintains moderate computational complexity, thanks to compact transition functions $H_i^m(\cdot)$. For a given $i \in \{1, 2, \dots, L-1\}$, the set $\{x_i^n\}$ provides complementary information from other modalities to enhance the representation of modality m at $(i+1)$ -th CAB.

After all CABs, a residual connection mechanism is applied to aggregate x_L^m with the original input ($\mathbf{F}_{DF}^m + \mathbf{F}_0^m$) to calculate the final output \mathbf{F}_{Fused}^m as

$$\mathbf{F}_{Fused}^m = \alpha \cdot x_L^m + (\mathbf{F}_{DF}^m + \mathbf{F}_0^m),$$

where α is a learnable scaling factor to stabilize the training process.

Cross-Map Attention Block

To balance expressive ability and efficiency, our proposed CABs are implemented using efficient window attention. A Window-based Multi-head Cross-map Attention (W-MCA) mechanism is introduced to enable modality-aware interaction. Suppose input size is $H \times W \times C$, Swin Transformer (Liu et al. 2021) firstly partitions the input into $\frac{H \times W}{S^2} \times S^2 \times C$ non-overlapping $S \times S$ local windows. Given an embedding dimension d and a local window $X_m \in \mathbb{R}^{S^2 \times C}$ of current modality m , $\forall i \in \mathcal{M}$, the Query, Key and Value, Q_i , K_m and $V_m \in \mathbb{R}^{S^2 \times d}$ matrices are computed as

$$Q_i = X_i P_{Q_i}, K_m = X_m P_{K_m}, V_m = X_m P_{V_m},$$

where $X_i \in \mathbb{R}^{S^2 \times C}$ is the local window from all modalities \mathcal{M} ; P_{Q_i} , P_{K_m} and $P_{V_m} \in \mathbb{R}^{C \times d}$ are linear projection matrices shared across different windows. Note that P_{K_m} and P_{V_m} are applied only to the local window input X_m of modality m , while P_{Q_i} is specific to each query modality i , being applied to its corresponding local window input X_i .

For $m \in \mathcal{M}$, the cross-map attention is calculated as

$$\text{Attn}_m = \sum_{i \in \mathcal{M}} \text{SoftMax} \left(\frac{Q_i (K_m)^T}{\sqrt{d}} + b_i \right) V_m,$$

where b_i is a learnable relative positional encoding.

Fused Feature Extraction

Compared with late fusion, intermediate fusion presents better effectiveness in capturing complex interactions between different modalities in deep learning (Boulahia et al. 2021; Guarrasi et al. 2025). Instead of merging features only at the final reconstruction stage, intermediate fusion encourages early and repeated interactions across different modalities, allowing the model to learn richer representation of features.

To leverage this advantage, for modality m , a modality-specific Fused Feature Extraction module $H_{FEE}^m(\cdot)$ is attached immediately after the Cross-Map Feature Fusion module. This module extracts refined representations from its own fused feature \mathbf{F}_{Fused}^m , while preserving multi-modal contextual benefits inherited from the Cross-Map Feature Fusion module. It is worth noting that $H_{FEE}^m(\cdot)$ is a modular and flexible component, aligning with any Deep Feature Extraction architecture employed in Swin-transformer-based SISR models. It can be initialized by those pre-trained SISR models to provide a better starting point and accelerate convergence. This plug-and-play manner allows freely choosing a suitable architecture in terms of computational cost, inference time and reconstruction accuracy. As an example shown in fig. 3, the Residual Hybrid Transformer Block (RHTB) from HMANet (Chu et al. 2024) is adopted as base residual transformer block of proposed $H_{FEE}^m(\cdot)$.

Loss Function

A two terms total loss function to supervise the learning of PBR material super-resolution process is defined as

$$\mathcal{L}_{total} = \mathcal{L}_{rec} + \mathcal{L}_{mat},$$

where \mathcal{L}_{rec} denotes the reconstruction loss based on rendering appearance and \mathcal{L}_{mat} refers to the PBR material map loss that directly compares reconstructed SR material maps with ground-truth.

Reconstruction Loss. To calculate reconstruction loss \mathcal{L}_{rec} under consistent illumination, both the SR material maps and ground-truth are rendered under a set Ω of single point light sources, uniformly sampled from the hemisphere based on the Fibonacci sampling strategy. The \mathcal{L}_{rec} is then computed between resulting renderings by measuring both pixel-wise and perceptual differences as below

$$\begin{aligned} \mathcal{L}_{rec} = & \sum_{\omega_i \in \Omega} \mathcal{L}_{1c} (R^{\omega_i}(\mathcal{M}_{gt}), R^{\omega_i}(\mathcal{M}_{sr})) \\ & + \sum_{\omega_i \in \Omega} \mathcal{L}_{VGG-11} (R^{\omega_i}(\mathcal{M}_{gt}), R^{\omega_i}(\mathcal{M}_{sr})), \end{aligned}$$

where $R^{\omega_i}\{\cdot\}$ denotes rendering under single point light $\omega_i \in \Omega$; \mathcal{L}_{1c} is the Charbonnier (Lai et al. 2018; Charbonnier et al. 1994; Anagun, Isik, and Seke 2019) loss for pixel-wise differences and \mathcal{L}_{VGG-11} is the perceptual loss (Johnson, Alahi, and Fei-Fei 2016; Ledig et al. 2017a; Wu et al. 2017; Rad et al. 2019; Zhang et al. 2018a) calculating the differences between features extracted from a pre-trained VGG11 network (Simonyan and Zisserman 2014); \mathcal{M}_{gt} and \mathcal{M}_{sr} are the sets of ground-truth material maps and SR material maps, respectively.

Material Loss. In parallel, material loss \mathcal{L}_{mat} is introduced to directly compare SR material maps with ground-truth without rendering. It is formulated including both pixel-wise and perceptual loss as

$$\begin{aligned} \mathcal{L}_{mat} = & \sum_{m \in \mathcal{M}} \mathcal{L}_{1c} (m_{gt}, m_{sr}) \\ & + \sum_{m \in \mathcal{M}} \mathcal{L}_{VGG-11} (m_{gt}, m_{sr}), \end{aligned}$$

where m_{gt} and m_{sr} respectively denote the ground-truth and SR material maps for each map m in \mathcal{M} .

The definitions of above Charbonnier and perceptual losses are explained as follows.

Charbonnier Loss. The Charbonnier loss (Lai et al. 2018; Charbonnier et al. 1994; Anagun, Isik, and Seke 2019) is a robust and differentiable approximation of the $L1$ loss defined as

$$\mathcal{L}_{1c} = \sqrt{\|\mathbf{I}_{gt} - \mathbf{I}_{pred}\|_2^2 + \epsilon^2},$$

where ϵ is set to 10^{-3} ; \mathbf{I}_{gt} and \mathbf{I}_{pred} denote predicted result and ground-truth label respectively. The Charbonnier loss presents faster convergence than $L2$ loss and better robustness to outliers compared to the $L1$ loss.

Perceptual Loss. The perceptual loss has been widely adopted to train super-resolution models (Johnson, Alahi, and Fei-Fei 2016; Ledig et al. 2017a; Wu et al. 2017; Rad et al. 2019; Zhang et al. 2018a). Inspired by recent findings in image super-resolution research (Pihlgren et al. 2024), higher weights are assigned to shallower VGG11 layers to better capture high-frequency details such as textures and edges. The perceptual loss is defined as

$$\mathcal{L}_{VGG-11} = \sum_{i \in L} \lambda_i \cdot \mathcal{L}_{1c} (\phi_i(\mathbf{I}_{gt}), \phi_i(\mathbf{I}_{pred})),$$

where L denotes the set of selected convolutional layers in the pre-trained VGG11 network; $\phi_i(\cdot)$ denotes feature maps extracted from the i -th layer in L , and λ_i denotes the weight assigned to the i -th layer.

Experiments

Experimental Setup

In order to validate the performance of our method, we perform extensive experiments to compare it against existing SISR baselines using two different 2048×2048 resolution datasets, namely MatSynth (Vecchio and Deschaintre 2024) with 5,700 mixed quality assets for pre-training and our in-house dataset with 1,129 high quality and rich detailed assets for fine-tuning. LR versions of GT PBR materials are obtained by applying a bicubic down-sampling method with scale factors 0.5 and 0.25.

We randomly crop images into 64×64 patches for training with a batch size of 16 on one NVIDIA H100 (80GB). The number of CAB is set to 4 with 6 attention heads, and the window size of W-MCA is set to 8×8 . Fused Feature Extraction module is set to 3 depths with 6 attention heads in each. During pre-training based on MatSynth, the number of epochs is set to 170, and the learning rate is initialized to 1×10^{-4} and halved at 35%, 60%, 75% and 90%. During fine-tuning based on our in-house dataset, the number of epochs is set to 500 with a batch size of 16, and the initial learning rate is set to 4×10^{-5} and halved at 35%, 60%, 75% and 90%. The model is optimized using the Lion (Chen et al. 2023a) optimizer.

We employ the same renderer for both training and evaluation, implementing the Cook-Torrance BRDF model (Cook and Torrance 1982) with:

- Trowbridge-Reitz GGX normal distribution (Trowbridge and Reitz 1975),
- Schlick-GGX geometry term (Karis and Games 2013),
- Schlick’s Fresnel approximation (Schlick 1994).

Unless otherwise specified, in order to ensure fairness and objectivity, the maps not involved in the SR process are replaced with the GT version during the rendering process.

Quantitative Comparison

Table 1 reports the quantitative comparison between MUI-CAs and SOTA SISR methods on both MatSynth and our in-house dataset. Evaluation is performed in terms of PSNR(dB), SSIM and LPIPS (Zhang et al. 2018a). PSNR

and SSIM assess pixel-level fidelity and structural similarity, while LPIPS serves as a perceptual metric aligned with human visual judgment. Those metrics provide a comprehensive and balanced assessment of both reconstruction accuracy and perceptual quality.

MUJICAs consistently achieves superior performance across all metrics and datasets. Notably, HMANet-MUJICA consistently outperforms SwinIR-MUJICA, reflecting the relative capability of their SISR backbones. For $\times 2$ SR task, MUJICAs outperform their corresponding SISR backbones with gains up to **1.15dB** in PSNR, **0.0069** in SSIM, and a reduction of **0.036** in LPIPS on renderings across datasets. For $\times 4$ SR task, MUJICAs improves metrics up to **0.76dB** in PSNR, **0.0070** in SSIM, and **0.0695** in LPIPS. These metrics demonstrate that MUJICA consistently outperforms existing SISR models.

Visual Comparison

Material Map Visual Comparison. As presented in fig. 4 and supp.mat fig.1, MUJICA reconstructs finer and more accurate details than its SISR backbone, demonstrating its superior restoration capability. This performance emphasizes the effectiveness of cross-map interactions in enhancing details reconstruction.

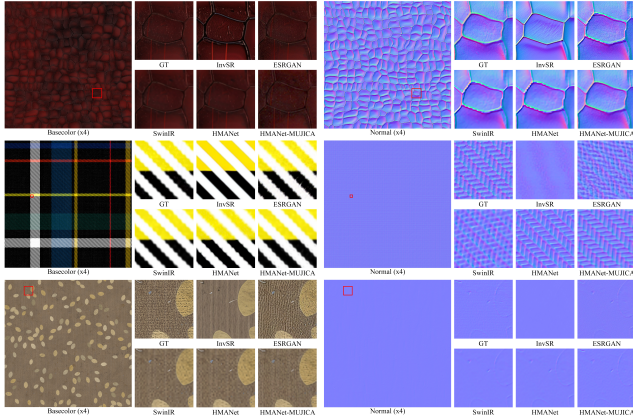


Figure 4: Material Map Visual Comparison. MUJICA outperforms other SISR methods in restoring more accurate and more detailed results.

Consistency Visual Comparison. To evaluate rendering consistency, we compare MUJICA with SISR baselines under varying lighting conditions. We use three single point lights selected from Fibonacci-sampled light sets. As demonstrated in fig. 5, supp.mat fig.2 and supp.mat fig.3, existing SISR models show visible inconsistencies under varying lighting conditions, revealing limitations in their per-map processing manner. In contrast, MUJICA maintains remarkable consistency while restoring better details.

Ablation Study

We choose SwinIR-MUJICA for ablation study based on MatSynth for both training and testing. The SR task is lim-

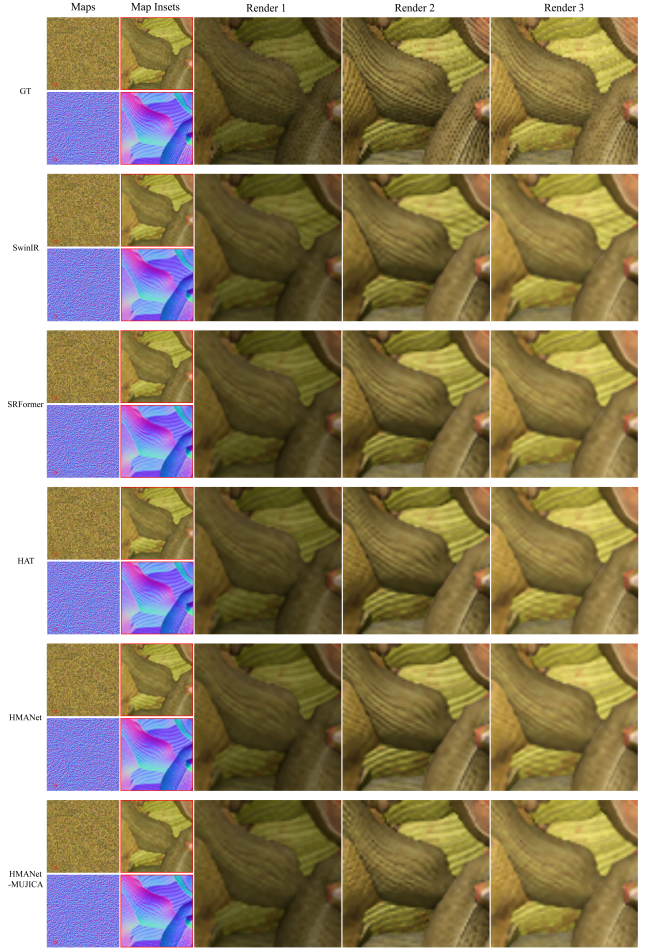


Figure 5: Consistency Visual Comparison. Only MUJICA preserves consistency under varying lighting conditions, while others present visible inconsistencies.

ited to $\times 2$. The number of epochs is set to 120 with a batch size of 8 and evaluation is based on a directional light.

Impact of Feature Fusion Method. We compare our proposed W-MCA with a baseline feature fusion method where the feature maps from different material maps are concatenated and then compressed via a convolution layer. As shown in table 2, replacing the concatenation operation with W-MCA leads to consistent improvements across all metrics, indicating the effectiveness of the attention-based fusion mechanism.

Methods	Rendering			Basecolor			Normal		
	PSNR \uparrow	SSIM \uparrow	LPIPS \downarrow	PSNR \uparrow	SSIM \uparrow	LPIPS \downarrow	PSNR \uparrow	SSIM \uparrow	LPIPS \downarrow
Concat + Conv	35.59	0.9205	0.0987	40.30	0.9473	0.0949	39.27	0.9472	0.0260
W-MCA	37.94	0.9374	0.0723	43.96	0.9614	0.0646	39.74	0.9492	0.0240

Table 2: Ablation study of different feature fusion methods.

Impact of CAB Count. Metrics of the table 3 demonstrate that the number of CABs is positively correlated with model performance. Employing 4 CABs provides a good trade-off between performance and computational cost.

Method	Scale	MatSynth (2024)									In-house Dataset								
		Rendering			Basecolor			Normal			Rendering			Basecolor			Normal		
		PSNR↑	SSIM↑	LPIPS↓	PSNR↑	SSIM↑	LPIPS↓	PSNR↑	SSIM↑	LPIPS↓	PSNR↑	SSIM↑	LPIPS↓	PSNR↑	SSIM↑	LPIPS↓	PSNR↑	SSIM↑	LPIPS↓
HAT (2023b)	×2	37.51	0.9359	0.0842	43.75	0.9624	0.0668	38.20	0.9404	0.0391	36.27	0.8963	0.1257	36.44	0.8843	0.1661	39.34	0.9425	0.0317
SRFormer (2023)	×2	37.29	0.9355	0.0859	43.72	0.9625	0.0674	37.81	0.9392	0.0402	36.03	0.8956	0.1286	36.29	0.8841	0.1688	38.77	0.9416	0.0322
SwinIR (2021)	×2	37.17	0.9332	0.0885	43.62	0.9621	0.0678	37.66	0.9359	0.0437	36.02	0.8939	0.1299	36.31	0.8837	0.1693	38.68	0.9386	0.0344
HMANet (2024)	×2	37.70	0.9375	0.0806	43.86	0.9629	0.0652	38.54	0.9430	0.0356	36.28	0.8986	0.1210	36.52	0.8856	0.1636	39.40	0.9451	0.0288
SwinIR-MUJICA	×2	37.77	0.9362	0.0672	43.63	0.9612	0.0561	39.38	0.9491	0.0230	37.17	0.9008	0.0980	36.94	0.8842	0.1420	43.26	0.9558	0.0135
HMANet-MUJICA	×2	38.21	0.9389	0.0613	44.26	0.9630	0.0486	39.46	0.9494	0.0239	37.38	0.9047	0.0850	37.15	0.8886	0.1185	43.90	0.9575	0.0127
ESRGAN (2018)	×4	31.98	0.7946	0.2923	38.93	0.8719	0.2301	32.57	0.7905	0.2108	32.78	0.7661	0.3302	33.57	0.7668	0.4203	35.19	0.8298	0.1710
SinSR (2024)	×4	24.06	0.4941	0.4436	28.03	0.6181	0.3963	24.58	0.5635	0.3022	24.53	0.4716	0.4202	25.65	0.4801	0.4380	25.72	0.6284	0.2801
InvSR (2025)	×4	23.75	0.5435	0.3948	26.73	0.6592	0.3707	25.17	0.6044	0.3842	24.05	0.5279	0.3817	24.20	0.5209	0.4197	26.85	0.6776	0.3082
ResShift (2023)	×4	27.94	0.6672	0.2530	33.32	0.7633	0.1877	28.37	0.7154	0.1512	28.70	0.6721	0.2031	30.10	0.6615	0.2113	29.32	0.7757	0.1324
HAT (2023b)	×4	32.13	0.8040	0.2719	38.58	0.8739	0.2235	32.79	0.8096	0.1870	32.82	0.7751	0.3167	33.41	0.7703	0.4089	34.81	0.8442	0.1547
SRFormer (2023)	×4	32.05	0.8029	0.2786	38.66	0.8742	0.2242	32.62	0.8062	0.1961	32.61	0.7735	0.3219	33.43	0.7694	0.4150	34.03	0.8421	0.1600
SwinIR (2021)	×4	31.99	0.7995	0.2795	38.52	0.8723	0.2236	32.59	0.8026	0.1976	32.68	0.7715	0.3229	33.37	0.7684	0.4126	34.23	0.8389	0.1591
DRCT (2024)	×4	31.97	0.7985	0.2878	38.40	0.8720	0.2264	32.60	0.7992	0.2080	32.72	0.7693	0.3282	33.38	0.7672	0.4157	34.51	0.8360	0.1708
HMANet (2024)	×4	32.37	0.8093	0.2702	38.73	0.8764	0.2203	33.20	0.8167	0.1869	32.85	0.7789	0.3139	33.46	0.7733	0.4030	34.79	0.8480	0.1554
SwinIR-MUJICA	×4	32.30	0.8041	0.2398	38.42	0.8678	0.2043	33.88	0.8293	0.1581	33.20	0.7783	0.2698	33.61	0.7737	0.3387	36.68	0.8580	0.1197
DRCT-MUJICA	×4	32.23	0.8022	0.2452	38.44	0.8662	0.2118	33.63	0.8263	0.1613	33.11	0.7762	0.2649	33.58	0.7734	0.3317	36.84	0.8579	0.1214
HMANet-MUJICA	×4	32.73	0.8148	0.2162	39.24	0.8773	0.1748	34.18	0.8334	0.1459	33.61	0.7859	0.2444	34.42	0.7828	0.3039	37.16	0.8622	0.1051

Table 1: Quantitative comparison on $\times 2$ and $\times 4$ PBR material SR task. We highlight the **best**, **second-best** and **third-best** for each metric. **Methods** with the suffix ”-MUJICA” indicate the application of MUJICA.

CABs	Rendering			Basecolor			Normal		
	PSNR↑	SSIM↑	LPIPS↓	PSNR↑	SSIM↑	LPIPS↓	PSNR↑	SSIM↑	LPIPS↓
2	37.84	0.9364	0.0728	43.77	0.9611	0.0659	39.64	0.9489	0.0241
4	37.94	0.9374	0.0723	43.96	0.9614	0.0646	39.74	0.9492	0.0240
6	38.07	0.9380	0.0719	44.08	0.9614	0.0644	39.73	0.9496	0.0248

Table 3: Ablation study of different number of CABs.

Impact of Connection Methods in CAB. Table 4 displays metrics of 3 different connection methods in CAB, which are No Residual Connection (NRC), Residual Connection (RC) and Dense Connection (DC). As shown in table 4, RC improves the performance over NRC, while DC further enhances results compared to RC alone.

Methods	Rendering			Basecolor			Normal		
	PSNR↑	SSIM↑	LPIPS↓	PSNR↑	SSIM↑	LPIPS↓	PSNR↑	SSIM↑	LPIPS↓
NRC	15.73	0.4795	0.8796	17.26	0.4456	0.7711	24.17	0.6054	0.6247
RC	37.79	0.9364	0.0727	43.81	0.9607	0.0653	39.69	0.9486	0.0247
DC	37.94	0.9374	0.0723	43.96	0.9614	0.0646	39.74	0.9492	0.0240

Table 4: Ablation study of different connection methods.

Impact of Fused Maps. Table 5 presents metrics of different map fusion combinations. Two specific combinations are investigated as below

- (a) Basecolor + Normal,
- (b) Basecolor + Normal + Roughness.

In combination (a), the roughness map is upscaled independently using the pre-trained SwinIR model. As demonstrated in table 5, (b) presents a better performance than (a) thanks to the complementary information from the roughness map, confirming the effectiveness of cross-map fusion. Nevertheless, (a) is employed for evaluation experiments because of its reduced computational overhead and lower resource demands.

Methods	Rendering			Basecolor			Normal			Roughness		
	PSNR↑	SSIM↑	LPIPS↓	PSNR↑	SSIM↑	LPIPS↓	PSNR↑	SSIM↑	LPIPS↓	PSNR↑	SSIM↑	LPIPS↓
(a)	37.85	0.9366	0.0740	43.96	0.9614	0.0646	39.74	0.9492	0.0240	34.64	0.8535	0.1877
(b)	37.91	0.9371	0.0733	43.99	0.9617	0.0637	39.81	0.9498	0.0232	34.91	0.8551	0.1556

Table 5: Ablation study of different map fusion combinations.

The metallic map, in contrast, typically appears as a constant (often black) image and lacks discriminative patterns.

Its distribution substantially diverges from other maps, making it less suitable for cross-map fusion. Consequently, it is excluded from our maps fusion combinations.

Conclusion

In this work, we propose Multi-modal Upscaling Joint Inference via Cross-map Attention (MUJICA), a flexible adapter that reforms pre-trained Swin-transformer-based SISR models for PBR material super-resolution. MUJICA is seamlessly attached after the pre-trained SISR backbone, which remains entirely frozen. It leverages cross-map attention to fuse features while preserving remarkable reconstruction ability of the pre-trained SISR model. Applied to SISR models such as SwinIR, DRCT and HMANet, MUJICA improves PSNR, SSIM, and LPIPS scores while preserving cross-map consistency. Experiments demonstrate that MUJICA enables efficient training even with limited resources and delivers state-of-the-art performance on PBR material datasets.

Limitations and Future Work

As demonstrated in table 5, incorporating the roughness map into cross-map fusion enhances overall performance at the cost of higher computational overhead and resource requirements. One possible way is to adopt distributed training for MUJICA including the roughness map in cross-map fusion, which could yield further improvements. Additionally, the FLIP loss (Andersson et al. 2021), which is theoretically better aligned with the PBR material SR, could replace the VGG-based perceptual loss to enhance performance. Finally, the core idea of cross-map fusion could be extended to other domains, such as intrinsic image decomposition, image delighting and PBR material decomposition.

References

- Anagun, Y.; Isik, S.; and Seke, E. 2019. SRLibrary: Comparing different loss functions for super-resolution over various convolutional architectures. *Journal of Visual Communication and Image Representation*, 61: 178–187.
- Andersson, P.; Nilsson, J.; Shirley, P.; and Akenine-Möller, T. 2021. Visualizing Errors in Rendered High Dynamic Range Images. In *Eurographics Short Papers*.
- Baltrušaitis, T.; Ahuja, C.; and Morency, L.-P. 2018. Multimodal machine learning: A survey and taxonomy. *IEEE transactions on pattern analysis and machine intelligence*, 41(2): 423–443.
- Boulahia, S. Y.; Amamra, A.; Madi, M. R.; and Daikh, S. 2021. Early, intermediate and late fusion strategies for robust deep learning-based multimodal action recognition. *Machine Vision and Applications*, 32(6): 121.
- Charbonnier, P.; Blanc-Feraud, L.; Aubert, G.; and Barlaud, M. 1994. Two deterministic half-quadratic regularization algorithms for computed imaging. In *Proceedings of 1st international conference on image processing*, volume 2, 168–172. IEEE.
- Chen, X.; Liang, C.; Huang, D.; Real, E.; Wang, K.; Pham, H.; Dong, X.; Luong, T.; Hsieh, C.-J.; Lu, Y.; and Le, Q. V. 2023a. Symbolic Discovery of Optimization Algorithms. In Oh, A.; Naumann, T.; Globerson, A.; Saenko, K.; Hardt, M.; and Levine, S., eds., *Advances in Neural Information Processing Systems*, volume 36, 49205–49233. Curran Associates, Inc.
- Chen, X.; Wang, X.; Zhang, W.; Kong, X.; Qiao, Y.; Zhou, J.; and Dong, C. 2023b. Hat: Hybrid attention transformer for image restoration. *arXiv preprint arXiv:2309.05239*.
- Chen, Y.; Nie, Y.; Ummenhofer, B.; Birkel, R.; Paulitsch, M.; and Nießner, M. 2025. PBR-SR: Mesh PBR Texture Super Resolution from 2D Image Priors. *arXiv preprint arXiv:2506.02846*.
- Chu, S.-C.; Dou, Z.-C.; Pan, J.-S.; Weng, S.; and Li, J. 2024. HMANet: Hybrid Multi-Axis Aggregation Network for Image Super-Resolution. In *Proceedings of the IEEE/CVF Conference on Computer Vision and Pattern Recognition (CVPR) Workshops*, 6257–6266.
- Cook, R. L.; and Torrance, K. E. 1982. A reflectance model for computer graphics. *ACM Transactions on Graphics (ToG)*, 1(1): 7–24.
- Esser, P.; Kulal, S.; Blattmann, A.; Entezari, R.; Müller, J.; Saini, H.; Levi, Y.; Lorenz, D.; Sauer, A.; Boesel, F.; et al. 2024. Scaling rectified flow transformers for high-resolution image synthesis. In *Forty-first international conference on machine learning*.
- Gauthier, A.; Kerbl, B.; Levallois, J.; Faury, R.; Thiery, J.-M.; and Boubekur, T. 2024. MatUp: Repurposing image upsamplers for SVBRDFs. In *Computer Graphics Forum*, volume 43, e15151. Wiley Online Library.
- Guarrasi, V.; Aksu, F.; Caruso, C. M.; Di Feola, F.; Rofena, A.; Ruffini, F.; and Soda, P. 2025. A systematic review of intermediate fusion in multimodal deep learning for biomedical applications. *Image and Vision Computing*, 105509.
- Gunes, H.; and Piccardi, M. 2005. Affect recognition from face and body: early fusion vs. late fusion. In *2005 IEEE international conference on systems, man and cybernetics*, volume 4, 3437–3443. IEEE.
- Guo, W.; Su, K.; Jiang, B.; Xie, K.; and Liu, J. 2024. CMDAF: Cross-Modality Dual-Attention Fusion Network for Multimodal Sentiment Analysis. *Applied Sciences*, 14(24): 12025.
- Ho, J.; Jain, A.; and Abbeel, P. 2020. Denoising diffusion probabilistic models. *Advances in neural information processing systems*, 33: 6840–6851.
- Hsu, C.-C.; Lee, C.-M.; and Chou, Y.-S. 2024. DRCT: Saving Image Super-Resolution Away from Information Bottleneck. In *Proceedings of the IEEE/CVF Conference on Computer Vision and Pattern Recognition (CVPR) Workshops*, 6133–6142.
- Huang, G.; Liu, Z.; van der Maaten, L.; and Weinberger, K. Q. 2017. Densely connected convolutional networks. In *Proceedings of the IEEE Conference on Computer Vision and Pattern Recognition*.
- Johnson, J.; Alahi, A.; and Fei-Fei, L. 2016. Perceptual losses for real-time style transfer and super-resolution. In *European conference on computer vision*, 694–711. Springer.
- Karis, B.; and Games, E. 2013. Real shading in unreal engine 4. *Proc. Physically Based Shading Theory Practice*, 4(3): 1.
- Lai, W.-S.; Huang, J.-B.; Ahuja, N.; and Yang, M.-H. 2018. Fast and accurate image super-resolution with deep laplacian pyramid networks. *IEEE transactions on pattern analysis and machine intelligence*, 41(11): 2599–2613.
- Ledig, C.; Theis, L.; Huszár, F.; Caballero, J.; Cunningham, A.; Acosta, A.; Aitken, A.; Tejani, A.; Totz, J.; Wang, Z.; et al. 2017a. Photo-realistic single image super-resolution using a generative adversarial network. In *Proceedings of the IEEE conference on computer vision and pattern recognition*, 4681–4690.
- Ledig, C.; Theis, L.; Huszár, F.; Caballero, J.; Cunningham, A.; Acosta, A.; Aitken, A.; Tejani, A.; Totz, J.; Wang, Z.; and Shi, W. 2017b. Photo-Realistic Single Image Super-Resolution Using a Generative Adversarial Network. In *2017 IEEE Conference on Computer Vision and Pattern Recognition (CVPR)*, 105–114.
- Li, H.; Yang, Y.; Chang, M.; Chen, S.; Feng, H.; Xu, Z.; Li, Q.; and Chen, Y. 2022. Srdiff: Single image super-resolution with diffusion probabilistic models. *Neurocomputing*, 479: 47–59.
- Li, S.; and Tang, H. 2024. Multimodal Alignment and Fusion: A Survey. *arXiv preprint arXiv:2411.17040*.
- Li, W.; Zhou, K.; Qi, L.; Jiang, N.; Lu, J.; and Jia, J. 2020. LAPAR: Linearly-Assembled Pixel-Adaptive Regression Network for Single Image Super-resolution and Beyond. In Larochele, H.; Ranzato, M.; Hadsell, R.; Balcan, M.; and Lin, H., eds., *Advances in Neural Information Processing Systems*, volume 33, 20343–20355. Curran Associates, Inc.

- Liang, J.; Cao, J.; Sun, G.; Zhang, K.; Van Gool, L.; and Timofte, R. 2021. SwinIR: Image Restoration Using Swin Transformer. In *2021 IEEE/CVF International Conference on Computer Vision Workshops (ICCVW)*, 1833–1844.
- Lim, B.; Son, S.; Kim, H.; Nah, S.; and Lee, K. M. 2017. Enhanced Deep Residual Networks for Single Image Super-Resolution. In *The IEEE Conference on Computer Vision and Pattern Recognition (CVPR) Workshops*.
- Liu, Z.; Lin, Y.; Cao, Y.; Hu, H.; Wei, Y.; Zhang, Z.; Lin, S.; and Guo, B. 2021. Swin transformer: Hierarchical vision transformer using shifted windows. In *Proceedings of the IEEE/CVF international conference on computer vision*, 10012–10022.
- Pihlgren, G. G.; Nikolaidou, K.; Chhipa, P. C.; Abid, N.; Saini, R.; Sandin, F.; and Liwicki, M. 2024. A Systematic Performance Analysis of Deep Perceptual Loss Networks: Breaking Transfer Learning Conventions. *arXiv:2302.04032*.
- Podell, D.; English, Z.; Lacey, K.; Blattmann, A.; Dockhorn, T.; Müller, J.; Penna, J.; and Rombach, R. 2023. Sdxl: Improving latent diffusion models for high-resolution image synthesis. *arXiv preprint arXiv:2307.01952*.
- Rad, M. S.; Bozorgtabar, B.; Marti, U.-V.; Basler, M.; Ekenel, H. K.; and Thiran, J.-P. 2019. Srobb: Targeted perceptual loss for single image super-resolution. In *Proceedings of the IEEE/CVF international conference on computer vision*, 2710–2719.
- Saharia, C.; Ho, J.; Chan, W.; Salimans, T.; Fleet, D. J.; and Norouzi, M. 2022. Image super-resolution via iterative refinement. *IEEE transactions on pattern analysis and machine intelligence*, 45(4): 4713–4726.
- Saravanan, D.; et al. 2025. A Generative Approach to High Fidelity 3D Reconstruction from Text Data. *arXiv preprint arXiv:2503.03664*.
- Schlick, C. 1994. An inexpensive BRDF model for physically-based rendering. In *Computer graphics forum*, volume 13, 233–246. Wiley Online Library.
- Shang, S.; Shan, Z.; Liu, G.; Wang, L.; Wang, X.; Zhang, Z.; and Zhang, J. 2024. Resdiff: Combining cnn and diffusion model for image super-resolution. In *Proceedings of the AAAI Conference on Artificial Intelligence*, volume 38, 8975–8983.
- Simonyan, K.; and Zisserman, A. 2014. Very deep convolutional networks for large-scale image recognition. *arXiv preprint arXiv:1409.1556*.
- Snoek, C. G.; Worring, M.; and Smeulders, A. W. 2005. Early versus late fusion in semantic video analysis. In *Proceedings of the 13th annual ACM international conference on Multimedia*, 399–402.
- Sohl-Dickstein, J.; Weiss, E.; Maheswaranathan, N.; and Ganguli, S. 2015. Deep unsupervised learning using nonequilibrium thermodynamics. In *International conference on machine learning*, 2256–2265. pmlr.
- Song, Y.; and Ermon, S. 2019. Generative modeling by estimating gradients of the data distribution. *Advances in neural information processing systems*, 32.
- Song, Y.; Sohl-Dickstein, J.; Kingma, D. P.; Kumar, A.; Ermon, S.; and Poole, B. 2020. Score-based generative modeling through stochastic differential equations. *arXiv preprint arXiv:2011.13456*.
- Trowbridge, T.; and Reitz, K. P. 1975. Average irregularity representation of a rough surface for ray reflection. *Journal of the optical society of America*, 65(5): 531–536.
- Tsai, Y.-H. H.; Bai, S.; Liang, P. P.; Kolter, J. Z.; Morency, L.-P.; and Salakhutdinov, R. 2019. Multimodal transformer for unaligned multimodal language sequences. In *Proceedings of the conference. Association for computational linguistics. Meeting*, volume 2019, 6558.
- Vaswani, A.; Shazeer, N.; Parmar, N.; Uszkoreit, J.; Jones, L.; Gomez, A. N.; Kaiser, Ł.; and Polosukhin, I. 2017. Attention is all you need. *Advances in neural information processing systems*, 30.
- Vecchio, G.; and Deschaintre, V. 2024. Matsynth: A modern pbr materials dataset. In *Proceedings of the IEEE/CVF Conference on Computer Vision and Pattern Recognition*, 22109–22118.
- Vecchio, G.; Martin, R.; Roullier, A.; Kaiser, A.; Rouffet, R.; Deschaintre, V.; and Boubekur, T. 2024a. Controlmat: a controlled generative approach to material capture. *ACM Transactions on Graphics*, 43(5): 1–17.
- Vecchio, G.; Sortino, R.; Palazzo, S.; and Spampinato, C. 2024b. Matfuse: controllable material generation with diffusion models. In *Proceedings of the IEEE/CVF Conference on Computer Vision and Pattern Recognition*, 4429–4438.
- Wang, X.; Yu, K.; Wu, S.; Gu, J.; Liu, Y.; Dong, C.; Qiao, Y.; and Loy, C. C. 2018. ESRGAN: Enhanced super-resolution generative adversarial networks. In *The European Conference on Computer Vision Workshops (ECCVW)*.
- Wang, Y.; Yang, W.; Chen, X.; Wang, Y.; Guo, L.; Chau, L.-P.; Liu, Z.; Qiao, Y.; Kot, A. C.; and Wen, B. 2024. Sinsr: diffusion-based image super-resolution in a single step. In *Proceedings of the IEEE/CVF conference on computer vision and pattern recognition*, 25796–25805.
- Wu, B.; Duan, H.; Liu, Z.; and Sun, G. 2017. SRPGAN: perceptual generative adversarial network for single image super resolution. *arXiv preprint arXiv:1712.05927*.
- Xiao, T.; Singh, M.; Mintun, E.; Darrell, T.; Dollar, P.; and Girshick, R. 2021. Early Convolutions Help Transformers See Better. In Ranzato, M.; Beygelzimer, A.; Dauphin, Y.; Liang, P.; and Vaughan, J. W., eds., *Advances in Neural Information Processing Systems*, volume 34, 30392–30400. Curran Associates, Inc.
- Xu, B.; Wang, N.; Chen, T.; and Li, M. 2015. Empirical evaluation of rectified activations in convolutional network. *arXiv preprint arXiv:1505.00853*.
- Ye, C.; Qiu, L.; Gu, X.; Zuo, Q.; Wu, Y.; Dong, Z.; Bo, L.; Xiu, Y.; and Han, X. 2024. Stablenormal: Reducing diffusion variance for stable and sharp normal. *ACM Transactions on Graphics (TOG)*, 43(6): 1–18.
- Yue, Z.; Liao, K.; and Loy, C. C. 2025. Arbitrary-steps image super-resolution via diffusion inversion. In *Proceedings of the Computer Vision and Pattern Recognition Conference*, 23153–23163.

- Yue, Z.; Wang, J.; and Loy, C. C. 2023. Resshift: Efficient diffusion model for image super-resolution by residual shifting. *Advances in Neural Information Processing Systems*, 36: 13294–13307.
- Zhang, J.; Fan, D.-P.; Dai, Y.; Anwar, S.; Saleh, F. S.; Zhang, T.; and Barnes, N. 2020. UC-Net: Uncertainty inspired RGB-D saliency detection via conditional variational autoencoders. In *Proceedings of the IEEE/CVF conference on computer vision and pattern recognition*, 8582–8591.
- Zhang, J.; Lei, J.; Xie, W.; Fang, Z.; Li, Y.; and Du, Q. 2023. SuperYOLO: Super resolution assisted object detection in multimodal remote sensing imagery. *IEEE Transactions on Geoscience and Remote Sensing*, 61: 1–15.
- Zhang, K.; Liang, J.; Van Gool, L.; and Timofte, R. 2021. Designing a practical degradation model for deep blind image super-resolution. In *Proceedings of the IEEE/CVF international conference on computer vision*, 4791–4800.
- Zhang, R.; Isola, P.; Efros, A. A.; Shechtman, E.; and Wang, O. 2018a. The unreasonable effectiveness of deep features as a perceptual metric. In *Proceedings of the IEEE conference on computer vision and pattern recognition*, 586–595.
- Zhang, Y.; Li, K.; Li, K.; Wang, L.; Zhong, B.; and Fu, Y. 2018b. Image super-resolution using very deep residual channel attention networks. In *Proceedings of the European conference on computer vision (ECCV)*, 286–301.
- Zhao, X.; Zhang, L.; Pang, Y.; Lu, H.; and Zhang, L. 2020. A single stream network for robust and real-time RGB-D salient object detection. In *Computer Vision–ECCV 2020: 16th European Conference, Glasgow, UK, August 23–28, 2020, Proceedings, Part XXII 16*, 646–662. Springer.
- Zhou, Y.; Li, Z.; Guo, C.-L.; Bai, S.; Cheng, M.-M.; and Hou, Q. 2023. Srformer: Permuted self-attention for single image super-resolution. In *Proceedings of the IEEE/CVF international conference on computer vision*, 12780–12791.